Ultramicroscopy 239 (2022) 113548

Contents lists available at ScienceDirect

Ultramicroscopy

journal homepage: www.elsevier.com/locate/ultramic

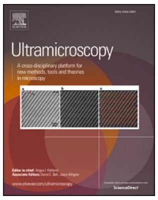

Quantum theory of magnon excitation by high energy electron beams

B.G. Mendis

Dept. of Physics, Durham University, South Road, Durham, DH1 3LE, UK

ARTICLE INFO

Keywords:
Magnons
Vortex beams
Electron diffraction
Electron energy loss spectroscopy

ABSTRACT

The role of magnon inelastic scattering in high energy electron diffraction of spin unpolarised electron beams, including vortex beams, is investigated theoretically for a Heisenberg ferromagnet. The interaction is between the atomic magnetic dipoles in the specimen and orbital angular momentum (OAM) of the electron beam. Magnon inelastic scattering by vortex beams is allowed despite many atoms along the magnon spin wave experiencing mixed OAM states. The scattering cross-section is however independent of the vortex beam winding number. In the case of planes waves in ferromagnetic iron, the magnon diffuse scattered intensity is significantly smaller than phonons in the energy loss range currently accessible by state-of-the-art monochromated electron energy loss spectroscopy (EELS). Nevertheless, it is shown that the long-range magnetic field of the atomic dipoles has a similar role to dipole scattering in phonon excitation. This means that magnons could, in principle, be detected using aloof beam EELS, where long acquisition times can be realised without any specimen beam damage, an important pre-requisite for detecting the weak magnon signal.

1. Introduction

Magnons are thermally excited spin waves that reduce the internal magnetisation of magnetic materials by creating spin misalignment [1]. For example, in a ground state ferromagnet all spins are parallel to one another, but in a magnon the spins precess about the ideal orientation in a spin wave pattern. This spin configuration is an excited state eigenfunction of the Hamiltonian and is equivalent to a coherent superposition of spin flips on each of the lattice sites [1]. Magnons share many similarities with phonons, i.e. both are massless bosons with a well-defined dispersion relationship. Phonons play a crucial role in high energy electron diffraction, such as the 'anomalous absorption' effect in diffraction contrast [2] and 'quasi-elastic' scattering in high angle annular dark filed (HAADF) imaging [3]. Recent advances in monochromation [4] have enabled phonon characterisation and mapping in materials [5–9] using electron energy loss spectroscopy (EELS). The quantum theory of phonon excitation was developed by Whelan [10] and more recently by Allen and co-workers [11–13].

Much less is known about the role of magnon scattering in electron microscopy. Phonons and magnons have similar energies in the meV range [14] and hence similar Bose-Einstein thermal populations. Magnon inelastic scattering could therefore potentially contribute to the diffuse background signal in electron diffraction, as well as be detected using high energy resolution EELS. A semi-classical, electrodynamic theory of magnetic inelastic scattering was recently developed by the author [15] and applied to magnons. This model demonstrated that vortex electron beams [16,17] are particularly suitable for magnon detection, since the strength of the magnetic interaction can be tuned by varying the orbital angular momentum (OAM), and therefore magnetic moment, of the vortex beam. The energy loss is due to the Stern-Gerlach force from an inhomogeneous magnetic field acting on the magnetic moment [15]. Although promising, the above results are based on a continuum description of the magnon, and a more realistic atomistic model using quantum mechanics is desirable.

In this work the quantum mechanical theory of magnon scattering in a Heisenberg ferromagnet is developed for high energy plane wave and vortex electron beams. The theory has some similarities to magnon scattering by neutron beams [18], which is due to the interaction between the neutron spin and atomic magnetic moments within the sample. However, here only spin unpolarised electron beams are considered, since this includes most current electron microscopes. The magnetic interaction is due to the OAM of the electron beam. Interestingly, the quantum mechanical model predicts magnon inelastic scattering of vortex beams is possible, despite the vortex beam being in a mixed OAM state for atoms outside the vortex centre. The scattering cross-section however is independent of vortex beam winding number, in direct contradiction to the electrodynamic model [15]. The magnetic diffuse scattered intensity and delocalisation in magnon excitation are also calculated, using ferromagnetic iron as an example. It is shown that for plane wave illumination the magnetic diffuse scattered intensity is significantly smaller than the thermal equivalent due to phonons, except at very small scattering angles, where the magnon energy is below the

---

E-mail address: b.g.mendis@durham.ac.uk.

https://doi.org/10.1016/j.ultramic.2022.113548
Received 2 December 2021; Received in revised form 25 April 2022; Accepted 4 May 2022

current energy resolution limit of monochromated EELS. Furthermore, the long-range magnetic field due to atomic dipoles in the solid gives rise to strong delocalisation at small scattering angles, similar to the long-range 'dipole' scattering in phonon excitation [19]. In principle, magnons could therefore be detected using EELS in aloof geometry, where the longer acquisition times would help detect the weak magnon signal without inducing any specimen beam damage.

2. Quantum mechanics of magnon scattering

The Hamiltonian $\hat{H}$ for the 'system' consisting of the spin unpolarised, high energy electron and ferromagnetic solid is given by:

$$\hat{H} = \hat{H}_0 + \frac{(\hat{\mathbf{p}} + e\hat{\mathbf{A}})^2}{2m} - eV \tag{1a}$$

$$V = \sum_N \frac{Ze}{4\pi\varepsilon_0|\mathbf{r}-\mathbf{r}_N|} - \sum_a \frac{e}{4\pi\varepsilon_0|\mathbf{r}-\mathbf{r}_a|} \tag{1b}$$

where $\hat{H}_0$ is the Hamiltonian for the ferromagnetic solid, m and e are the mass and magnitude of the charge of an electron and ε_0 is the permittivity of free space. V is the potential of the high energy electron which has position vector $\mathbf{r}$. The first term in Eq. (1b) is the Coulomb potential due to an atomic nucleus at position $\mathbf{r}_N$, while the second term is the Coulomb potential due to the atomic electrons (position vector $\mathbf{r}_a$). For simplicity, a monatomic solid with atomic number Z is assumed. The momentum operator is $\hat{\mathbf{p}} = -i\hbar\vec{\nabla}_{\mathbf{r}}$, where $\hbar$ is Planck's reduced constant and $\vec{\nabla}_{\mathbf{r}}$ is the del operator with respect to the variable $\mathbf{r}$. Treating individual atoms as magnetic dipoles, the magnetic vector potential operator $\hat{\mathbf{A}}$ can be expressed as [18]:

$$\hat{\mathbf{A}} = \frac{\mu_0}{4\pi}\sum_N\left[\hat{\boldsymbol{\mu}}_N \times \frac{\mathbf{r}-\mathbf{r}_N}{|\mathbf{r}-\mathbf{r}_N|^3}\right] = -\frac{\mu_0\gamma g\hbar}{4\pi}\sum_N\left[\hat{\mathbf{S}}_N \times \frac{\mathbf{r}-\mathbf{r}_N}{|\mathbf{r}-\mathbf{r}_N|^3}\right] \tag{2}$$

where μ_0 is the permeability of free space, and the magnetic moment operator of the N^{th}-atom, $\hat{\boldsymbol{\mu}}_N$, is due to its spin angular momentum operator $\hat{\mathbf{S}}_N$ (expressed in $\hbar$ units). $\gamma = e/2m$ is the gyromagnetic ratio and g is the Landé spin factor. In Eq. (2) the orbital angular momentum contribution of the atom is assumed to be small compared to the spin angular momentum; this is generally true of the transition metals due to orbital quenching [1]. It is easy to show that $\hat{\mathbf{p}}$ and $\hat{A}$ commute, i.e. $[\hat{\mathbf{p}},\hat{\mathbf{A}}] = \hat{p}\cdot\hat{A} - \hat{\mathbf{A}}\cdot\hat{p} = 0$. Substituting Eq. (2) in Eq. (1a) and ignoring the weaker $\hat{\mathbf{A}}^2$ term [1] gives:

$$\hat{H} = \hat{H}_0 - \frac{\hbar^2}{2m}\nabla_{\mathbf{r}}^2 - eV + i\left(\frac{\mu_0\mu_B^2}{\pi}\right)\sum_N\left[\hat{\mathbf{S}}_N \times \frac{\mathbf{r}-\mathbf{r}_N}{|\mathbf{r}-\mathbf{r}_N|^3}\right]\cdot\vec{\nabla}_{\mathbf{r}} \tag{3}$$

where $\mu_B = e\hbar/2m$ is the Bohr magneton and a value of 2 for g is reasonably assumed. The last term in Eq. (3) is the magnetic interaction of the electron beam with the solid. It is interesting to note that the summation term can also be expressed as:

$$\sum_N\left[\hat{\mathbf{S}}_N \times \frac{\mathbf{r}-\mathbf{r}_N}{|\mathbf{r}-\mathbf{r}_N|^3}\right]\cdot\vec{\nabla}_{\mathbf{r}} = \sum_N \hat{\mathbf{S}}_N\cdot\frac{\left[(\mathbf{r}-\mathbf{r}_N)\times\vec{\nabla}_{\mathbf{r}}\right]}{|\mathbf{r}-\mathbf{r}_N|^3} \tag{4}$$

The cross-product within the square brackets on the right-hand side has the same form as the orbital angular momentum operator for the electron beam with respect to the N^{th}-atom. The OAM for an electron vortex beam is well-defined for an atom located at its centre. However, for any other atom the vortex beam is not in a pure OAM state, and effectively consists of multiple OAM values of different weighting [20, 21]. Since both positive and negative OAM values are involved, it is not immediately clear if vortex beams can interact with magnons; similar considerations apply to the electron magnetic circular dichroism (EMCD) signal from individual atoms in a solid [22].

The system wavefunction (Ψ_s) for the Hamiltonian in Eq. (1a) can be expressed as:

$$\Psi_s(\mathbf{r},\mathbf{r}_a) = \sum_i u_i(\mathbf{r}_a)\Phi_i(\mathbf{r}) \tag{5}$$

where $\hat{H}_0 u_i = E_i u_i$ is the Schrödinger equation for the ferromagnetic solid in the i^{th}-state (energy E_i), with $i = 0$ being the ground state and $i > 0$ representing excited states. $\Phi_i(\mathbf{r})$ is the corresponding wavefunction for the high energy electron. Substituting Eq. (5) in Eq. (1a), multiplying by the complex conjugate u_f^* and integrating over $\mathbf{r}_a$ coordinates leads to:

$$\left[\nabla_{\mathbf{r}}^2 + 4\pi^2 k_f^2 - \frac{2me}{\hbar^2}H_{ff}(\mathbf{r})\right]\Phi_f(\mathbf{r}) = \frac{2me}{\hbar^2}\sum_{i\neq f}H_{fi}(\mathbf{r})\Phi_i(\mathbf{r}) \tag{6a}$$

$$H_{fi}(\mathbf{r}) = \int u_f^*(\mathbf{r}_a)\left[-V + i\left(\frac{\mu_0\mu_B^2}{\pi e}\right)\sum_N\left(\hat{\mathbf{S}}_N \times \frac{\mathbf{r}-\mathbf{r}_N}{|\mathbf{r}-\mathbf{r}_N|^3}\right)\cdot\vec{\nabla}_{\mathbf{r}}\right]u_i(\mathbf{r}_a)d\mathbf{r}_a \tag{6b}$$

with k_f being the high energy electron wavenumber for Φ_f with energy loss $(E_f - E_0)$. Eq. (6a) is derived by making use of the orthornormal property of the u_i eigenfunctions. H_{fi} is the matrix element for the transition from the initial (i) to final (f) state of the solid. The first term within the square brackets of Eq. (6b) represents electronic transitions, such as EELS core loss edges [23], and phonon excitations [11]. The second term corresponds to magnetic transitions. The right-hand side of Eq. (6a) signifies inelastic scattering from the different source terms Φ_i. Here the Born approximation is assumed to simplify the calculation, i.e. only the elastic beam Φ_0 has appreciable intensity. The Born approximation is valid for thin specimens where the scattering is weak. The square bracket terms on the left-hand side of Eq. (6a) denote elastic propagation of the Φ_f wave through the crystal. Ignoring $H_{ff}(\mathbf{r})$ mimics free space propagation by suppressing Bragg diffraction [24]. Under these conditions the inelastic scattered wavefunction is [25]:

$$\Phi_f(\mathbf{r}) = -\frac{me}{2\pi\hbar^2}\int\frac{\exp(2\pi i k_f|\mathbf{r}-\mathbf{r}'|)}{|\mathbf{r}-\mathbf{r}'|}H_{f0}(\mathbf{r}')\Phi_0(\mathbf{r}')d\mathbf{r}' \tag{7}$$

Here the excited state f corresponds to a single magnon creation event. Since this is a purely magnetic interaction with the solid, the non-magnetic contribution to H_{f0}, i.e. the first term in Eq. (6b), must be zero (see Supplementary Material for a proof), so that only the magnetic contribution must be evaluated. Using the Holstein-Primakoff transformation [26] the spin momentum operator $\hat{\mathbf{S}}_N$ can be expressed via the boson creation ($b_N^\dagger$) and annihilation (b_N) operators for the N^{th}-atom site [18]:

$$\hat{S}_N^z = S - b_N^\dagger b_N \tag{8a}$$

$$\hat{S}_N^x = \sqrt{\frac{S}{2}\left(1 - \frac{b_N^\dagger b_N}{2S}\right)}(b_N^\dagger + b_N) \approx \sqrt{\frac{S}{2}}(b_N^\dagger + b_N) \tag{8b}$$

$$\hat{S}_N^y = i\sqrt{\frac{S}{2}\left(1 - \frac{b_N^\dagger b_N}{2S}\right)}(b_N^\dagger - b_N) \approx i\sqrt{\frac{S}{2}}(b_N^\dagger - b_N) \tag{8c}$$

where S is the magnitude of the spin angular momentum (assumed identical for all atom sites) and $b_N^\dagger b_N$ is the number of spin 'flips' along the negative z-axis on the N^{th}-atom site, which is assumed to be small, leading to the approximations in Eqs. (8b) and (8c). For a magnon spin wave the boson operators can be expressed in reciprocal space [26]:

$$b_N^\dagger = \frac{1}{\sqrt{N_T}}\sum_{\mathbf{k}_m} e^{-2\pi i\mathbf{k}_m\cdot\mathbf{r}_N} b_{\mathbf{k}m}^\dagger \tag{9a}$$

$$b_N = \frac{1}{\sqrt{N_T}}\sum_{\mathbf{k}_m} e^{2\pi i\mathbf{k}_m\cdot\mathbf{r}_N} b_{\mathbf{k}m} \tag{9b}$$

with $\mathbf{k}_m$ being the magnon wavevector and $b_{\mathbf{k}m}^\dagger$, $b_{\mathbf{k}m}$ the boson creation and annihilation operators in reciprocal space. N_T is the total number of atom sites. Eqs. (8a)–(8c), (9a) and (9b) can be substituted in Eq. (6b) to calculate the magnetic transition potential. For single magnon creation events only 'unmixed' terms in $b_{\mathbf{k}m}^\dagger$ need be considered (this includes $\widehat{S}_N^x$ and $\widehat{S}_N^y$, but not $\widehat{S}_N^z$ which contains 'mixed' terms of the form $b_{\mathbf{k}m}^\dagger b_{\mathbf{k}'m}$; Eqs. (8a)–(8c). Note that if the focus was on energy unfiltered electron diffraction then unmixed terms in $b_{\mathbf{k}m}^\dagger$ and $b_{-\mathbf{k}m}$ must both be taken into account. This is because scattering along a vector $-\mathbf{k}_m$ can be due to either creation of a magnon with opposite wavevector $\mathbf{k}_m$ or destruction of a magnon with wavevector $-\mathbf{k}_m$ [10]. Nevertheless, due to the principle of detailed balance [8], energy gain events involving magnon annihilation are significantly less likely than magnon creation, and can therefore be ignored. For unmixed terms in $b_{\mathbf{k}m}^\dagger$ the summation over N in Eq. (6b) results in expressions of the form:

$$\sum_N e^{-2\pi i\mathbf{k}_m\cdot\mathbf{r}_N}\frac{(x-x_N)}{|\mathbf{r}-\mathbf{r}_N|^3} \rightarrow -\frac{e^{-2\pi i\mathbf{k}_m\cdot\mathbf{r}}}{V_o}\int\frac{(x_N-x)}{|\mathbf{r}_N-\mathbf{r}|^3}e^{-2\pi i\mathbf{k}_m\cdot(\mathbf{r}_N-\mathbf{r})}d(\mathbf{r}_N-\mathbf{r}) \tag{10}$$

The spacing between the atom sites is much smaller than the volume of the solid, which allows the discrete summation in Eq. (10) to be replaced with an integral. For atoms arranged in a simple cubic geometry the normalisation constant V_o is equal to the unit cell volume. For large N the integral is the Fourier transform of $(x_N - x)/|\mathbf{r}_N - \mathbf{r}|^3$. It can be evaluated using the method outlined in [27], which starts with the Fourier transform of the Coulomb potential, i.e.:

$$\int\frac{e^{-2\pi i\mathbf{k}_m\cdot(\mathbf{r}_N-\mathbf{r})}}{|\mathbf{r}_N-\mathbf{r}|}d(\mathbf{r}_N-\mathbf{r}) = \frac{1}{\pi k_m^2} \tag{11}$$

Inverse Fourier transforming and differentiating with respect to $(x_N - x)$ gives:

$$-\frac{(x_N-x)}{|\mathbf{r}_N-\mathbf{r}|^3} = \int\frac{2ik_{mx}}{k_m^2}e^{2\pi i\mathbf{k}_m\cdot(\mathbf{r}_N-\mathbf{r})}d\mathbf{k}_m \tag{12}$$

where k_{mx} is the x-component of the wavevector $\mathbf{k}_m$. It is clear that the Fourier transform of $(x_N - x)/|\mathbf{r}_N - \mathbf{r}|^3$ is $-(2ik_{mx}/k_m^2)$. Expressions equivalent to Eq. (10) with $(y - y_N)$ or $(z - z_N)$ replacing $(x - x_N)$ are also obtained from Eq. (6b). These can be evaluated using the same procedure. The magnetic part of the transition matrix element for single magnon creation is therefore:

$$H_{f0}^{\mathrm{mag}}(\mathbf{r}) = \left(\frac{\mu_0\mu_B^2}{\pi e V_o k_m^2}\right)\sqrt{\frac{2S(N_{km}+1)}{N_T}}e^{-2\pi i\mathbf{k}_m\cdot\mathbf{r}}\left[k_{mz}\left(\frac{\partial}{\partial y}-i\frac{\partial}{\partial x}\right)-\left(k_{my}-ik_{mx}\right)\frac{\partial}{\partial z}\right] \tag{13}$$

where k_{mz} and k_{my} are the z and y-components of the magnon wavevector $\mathbf{k}_m$. In deriving Eq. (13) use is made of the standard properties of a creation operator, i.e. $b_{\mathbf{k}m}^\dagger|u_0\rangle = \sqrt{N_{km}+1}|u_f\rangle$, where N_{km} is the number of magnons with wavevector $\mathbf{k}_m$ in the initial state $|u_0\rangle$ and $|u_f\rangle$ is the eigenfunction after single magnon creation.

Eqs. (7) and (13) indicate that spatial gradients in the wavefunction Φ_0 govern magnon scattering. It is instructive to consider the gradient terms separately. Starting with the $\partial/\partial z$ term, its contribution Φ_f^1 to the scattered wavefunction in Eq. (7) is:

$$\Phi_f^1(\mathbf{r}) = \left(\frac{m\mu_0\mu_B^2}{2\pi^2 V_o\hbar^2 k_m^2}\right)\sqrt{\frac{2S(N_{km}+1)}{N_T}}\int\frac{e^{2\pi ik_f|\mathbf{r}-\mathbf{r}'|}e^{-2\pi i\mathbf{k}_m\cdot\mathbf{r}'}}{|\mathbf{r}-\mathbf{r}'|}\left(k_{my}-ik_{mx}\right)\frac{\partial\Phi_0(\mathbf{r}')}{\partial z'}d\mathbf{r}' \tag{14}$$

In the far-field, i.e. $r\rightarrow\infty$, it is desirable to reduce Eq. (14) to the asymptotic form $(e^{2\pi ik_f r}/r)f_1(\theta,\ \phi)$, where $(e^{2\pi ik_f r}/r)$ is an outgoing spherical wave and $f_1(\theta,\phi)$ is the scattering factor in the direction of scattering, which has polar and azimuthal angles θ and ϕ respectively. Furthermore, $|\mathbf{r}-\mathbf{r}'| \approx r - \mathbf{n}\cdot\mathbf{r}'$, where $\mathbf{n}$ is the unit vector along the scattered direction (Fig. 1a). This result is valid so long as $|\mathbf{r}| \gg |\mathbf{r}'|$, which is a reasonable assumption, since from Eq. (14) the integration domain over $\mathbf{r}'$ is limited to the electron beam size $\Phi_0(\mathbf{r}')$. In the far-field Eq. (14) therefore simplifies to:

$$\Phi_f^1(\mathbf{r}) = \left(\frac{m\mu_0\mu_B^2}{2\pi^2 V_o\hbar^2 k_m^2}\right)\sqrt{\frac{2S(N_{km}+1)}{N_T}}\left(\frac{e^{2\pi ik_f r}}{r}\right)\int e^{-2\pi i\left(\mathbf{k}_f+\mathbf{k}_m\right)\cdot\mathbf{r}'}\left(k_{my}-ik_{mx}\right)\frac{\partial\Phi_0(\mathbf{r}')}{\partial z'}d\mathbf{r}' \tag{15}$$

where the $|\mathbf{r}-\mathbf{r}'|$ term in the denominator of Eq. (14) has been replaced with r to give the correct asymptotic form for Φ_f^1. Consider a vortex Bessel beam, $\Phi_0(\mathbf{r}') = J_\alpha(2\pi k_{i\perp}\rho')e^{i\alpha\phi'}e^{2\pi ik_{iz}z'}$, with winding number α and wavevector components $\mathbf{k}_{i\perp}, k_{iz}$ perpendicular and parallel to the optic z-axis respectively. J_α is a Bessel function of the first kind and (ρ', ϕ', z') are the cylindrical coordinates of $\mathbf{r}'$. The integral in Eq. (15) is then:

$$\begin{aligned}2\pi ik_{iz}\int e^{-2\pi i\left(\mathbf{k}_f+\mathbf{k}_m\right)\cdot\mathbf{r}'}\left(k_{my}-ik_{mx}\right)\Phi_0(\mathbf{r}')\rho'd\rho'd\phi'dz' &= 2\pi ik_{iz}\delta\left(k_{iz}-k_{fz}-k_{mz}\right)\\ \times\int e^{-2\pi i\left(\mathbf{k}_{f\perp}+\mathbf{k}_{m\perp}\right)\cdot\boldsymbol{\rho}'}\left(k_{my}-ik_{mx}\right)J_\alpha(2\pi k_{i\perp}\rho')e^{i\alpha\phi'}\rho'd\rho'd\phi'\end{aligned} \tag{16}$$

where $\mathbf{k}_{f\perp}, \mathbf{k}_{m\perp}$ and $\boldsymbol{\rho}'$ are the components of $\mathbf{k}_f$, $\mathbf{k}_m$ and $\mathbf{r}'$ perpendicular to the optic z-axis. The delta function on the right-hand side of Eq. (16) is a result of integrating over z'. It signifies conservation of linear momentum along the z-axis, consistent with the requirement that for creating a magnon with wavevector $\mathbf{k}_m$ the scattering vector must be $-\mathbf{k}_m$ (Fig. 1b). Anticipating linear momentum conservation perpendicular to the z-axis, we have [28]:

$$e^{-2\pi i\left(\mathbf{k}_{f\perp}+\mathbf{k}_{m\perp}\right)\cdot\boldsymbol{\rho}'} = e^{-2\pi i\mathbf{k}_{i\perp}\cdot\boldsymbol{\rho}'} = e^{-2\pi ik_{i\perp}\rho'\cos\phi'} = \sum_{n=-\infty}^{\infty}(-i)^n J_n(2\pi k_{i\perp}\rho')e^{in\phi'} \tag{17}$$

where the series expansion arbitrarily sets the x'-axis to be along $\mathbf{k}_{i\perp}$. Substituting in the right-hand side of Eq. (16) and performing the integration over ϕ' gives the following expression (note that only the $n = -\alpha$ term in Eq. (17) results in a non-zero value):

$$\begin{aligned}&\frac{4\pi^2}{i^{\alpha-1}}k_{iz}\left(k_{my}-ik_{mx}\right)\delta\left(k_{iz}-k_{fz}-k_{mz}\right)\int[J_\alpha(2\pi k_{i\perp}\rho')]^2\rho'd\rho'\\ &= \frac{2\pi}{i^{\alpha-1}}\frac{k_{iz}}{k_{i\perp}^2}\left(k_{my}-ik_{mx}\right)\delta\left(k_{iz}-k_{fz}-k_{mz}\right)\end{aligned} \tag{18}$$

When deriving Eq. (18), the result $J_{-\alpha}(2\pi k_{i\perp}\rho') = (-1)^\alpha J_\alpha(2\pi k_{i\perp}\rho')$, valid for integer α [28], and the relationship $\int_0^\infty [J_\alpha(2\pi k_{i\perp}\rho')]^2(k_{i\perp}\rho')d(k_{i\perp}\rho') = \delta(0)/2\pi$ has been used. The latter is, strictly speaking,

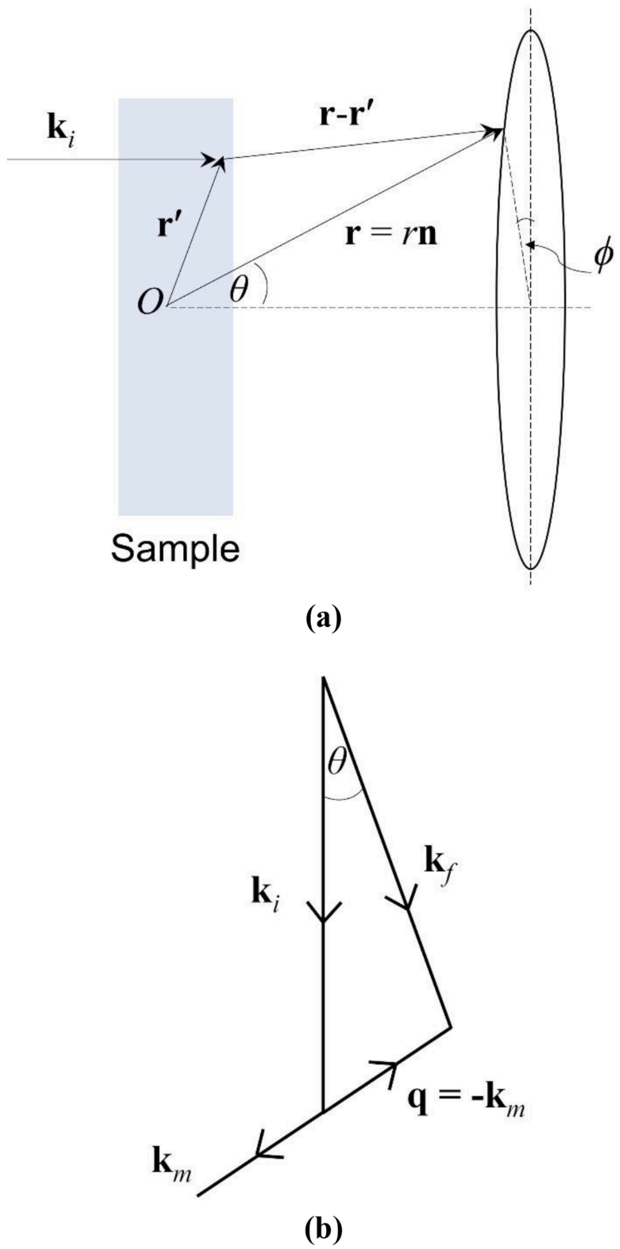

Fig. 1. (a) Schematic of the scattering geometry used for far-field calculations. Electrons with incident wavevector $\mathbf{k}_i$ are scattered from point $\mathbf{r}'$ within the sample (origin O). The intensity is calculated at a distance r along the unit vector $\mathbf{n}$, which corresponds to polar θ and azimuthal ϕ scattering angles. (b) Wavevector schematic for magnon scattering. The incident and scattered electron wavevectors are $\mathbf{k}_i$ and $\mathbf{k}_f$ respectively. The scattering vector $\mathbf{q}$ is anti-parallel to the magnon wavevector $\mathbf{k}_m$.

divergent due to the Dirac delta function. In practice however, the integral must remain finite, since it is proportional to the integrated intensity of the Bessel electron beam. This means that $\delta(0)$ must be replaced by a normalisation constant that is a function of the electron beam intensity. For simplicity the normalisation constant is taken to be unity, so that $\int_0^\infty [J_\alpha(2\pi k_{i\perp}\rho')]^2(k_{i\perp}\rho')d(k_{i\perp}\rho') = 1/2\pi$. Substituting in Eq. (15) we finally obtain:

$$\Phi_f^1(\mathbf{r}) = \left[\frac{1}{i^{\alpha-1}}\left(\frac{m\mu_0\mu_B^2}{\pi V_o\hbar^2 k_m^2}\right)\sqrt{\frac{2S(N_{km}+1)}{N_T}}\;\frac{k_{iz}\left(k_{my}-ik_{mx}\right)}{k_{i\perp}^2}\delta\left(k_{iz}-k_{fz}-k_{mz}\right)\right]\left(\frac{e^{2\pi i k_f r}}{r}\right) \tag{19}$$

The expression within the square bracket is $f_1(\theta,\phi)$. Note that $(k_{my}-ik_{mx})=-i|\mathbf{k}_{m\perp}|e^{i\phi}$; the azimuthal dependence means that Φ_m^1 has angular momentum $\hbar$, which together with the $-\hbar$ angular momentum of the magnon conserves angular momentum for the entire system. Importantly, the magnitude of $f_1(\theta,\phi)$ does not depend on the vortex winding number α, which implies that the incident electron beam need not possess the *net* angular momentum required for magnon creation. In fact, using the exact same procedure it can be shown that a plane wave incident along the optic axis, i.e. $\Phi_0(\mathbf{r})=e^{2\pi ik_iz}$, can also generate magnons, even though the net angular momentum along the z-direction is zero (see Eq. (27)). We may speculate on the mechanism of angular momentum transfer from the electron beam; in the case of a plane wave it is due to decomposition into individual angular momentum components (Eq. (17)), while for vortex beams the OAM 'mode broadening' effect observed for atoms outside the vortex centre is important [20,21]. Angular momentum transfer has also been discussed in the context of EMCD experiments using the more rigorous density matrix formalism [29]. It was shown that a plane wave can excite chiral electronic transitions in an atom with a corresponding change in angular momentum, although the angular momentum of the scattered electron is not a constant of motion, since radial symmetry is not preserved within the crystal [29]. In Eq. (19) however, $H_{mm}(\mathbf{r})$ and the crystal potential is ignored during propagation of the inelastic wave, so that the change in angular momentum is also observed in the far-field.

Next consider the $\partial/\partial x, \partial/\partial y$ terms in H_{f0}^{mag} (Eq. (13)). For a vortex Bessel beam, $\Phi_0(\mathbf{r})=J_\alpha(2\pi k_{i\perp}\rho)e^{i\alpha\phi}e^{2\pi ik_{iz}z}$, we obtain:

$$\frac{\partial\Phi_0}{\partial x}=\left[e^{i\alpha\phi}e^{2\pi ik_{iz}z}\frac{dJ_\alpha(2\pi k_{i\perp}\rho)}{d\rho}\right]\cos\phi-\frac{i\alpha}{\rho}\Phi_0\sin\phi \tag{20a}$$

$$\frac{\partial\Phi_0}{\partial y}=\left[e^{i\alpha\phi}e^{2\pi ik_{iz}z}\frac{dJ_\alpha(2\pi k_{i\perp}\rho)}{d\rho}\right]\sin\phi+\frac{i\alpha}{\rho}\Phi_0\cos\phi \tag{20b}$$

Substituting in Eqs. (7) and (13) the far-field scattered wavefunction Φ_f^2 is:

$$\Phi_f^2(\mathbf{r})=\left(\frac{m\mu_0\mu_B^2}{2\pi^2V_o\hbar^2k_m^2}\right)\sqrt{\frac{2S(N_{km}+1)}{N_T}}\left(\frac{e^{2\pi ik_fr}}{r}\right)k_{mz}$$
$$\times\int e^{-2\pi i\left(\mathbf{k}_f+\mathbf{k}_m\right)\cdot\mathbf{r}'}\left[ie^{i(\alpha+1)\phi'}\frac{dJ_\alpha(2\pi k_{i\perp}\rho')}{d\rho'}-\frac{i\alpha}{\rho'}e^{i(\alpha+1)\phi'}J_\alpha(2\pi k_{i\perp}\rho')\right]e^{2\pi ik_{iz}z'}\rho'd\rho'd\phi'dz' \tag{21}$$

Integrating over z' leads to the condition $k_{iz'}=k_{fz'}+k_{mz'}$, which signifies conservation of linear momentum along the optic axis. Substituting Eq. (17) in Eq. (21) and integrating over ϕ' gives:

$$\Phi_f^2(\mathbf{r})=\left\{\begin{array}{c}\left(\frac{m\mu_0\mu_B^2}{\pi V_o\hbar^2k_m^2}\right)\sqrt{\frac{2S(N_{km}+1)}{N_T}}\delta\left(k_{iz}-k_{fz}-k_{mz}\right)k_{mz}\times\\ \frac{1}{i^\alpha}\int\left[\rho'J_{\alpha+1}(2\pi k_{i\perp}\rho')\frac{dJ_\alpha(2\pi k_{i\perp}\rho')}{d\rho'}-\alpha J_\alpha(2\pi k_{i\perp}\rho')J_{\alpha+1}(2\pi k_{i\perp}\rho')\right]d\rho'\end{array}\right\}\left(\frac{e^{2\pi ik_fr}}{r}\right) \tag{22}$$

Using the expression for the derivative of a Bessel function [28]:

$$\frac{dJ_\alpha(2\pi k_{i\perp}\rho')}{d\rho'}=\frac{\alpha}{\rho'}J_\alpha(2\pi k_{i\perp}\rho')-2\pi k_{i\perp}J_{\alpha+1}(2\pi k_{i\perp}\rho') \tag{23}$$

it follows that:

$$\Phi_f^2(\mathbf{r})=\left[-\frac{1}{i^\alpha}\left(\frac{m\mu_0\mu_B^2}{\pi V_o\hbar^2k_m^2}\right)\sqrt{\frac{2S(N_{km}+1)}{N_T}}\;\frac{k_{mz}}{k_{i\perp}}\delta\left(k_{iz}-k_{fz}-k_{mz}\right)\right]\left(\frac{e^{2\pi ik_fr}}{r}\right) \tag{24}$$

The term within the square brackets is the scattering factor $f_2(\theta)$ for Φ_f^2; it is independent of ϕ, since the scattering depends only on the k_{mz} component. Since Φ_f^2 does not carry any angular momentum, but Φ_f^1 does, it follows that for a sample magnetised along the optic z-axis, magnons generated by the electron beam must have a wavevector component normal to the z-axis. This conclusion is consistent with the continuum electrodynamic model in [15], where the scattering cross-section is zero for magnons with zero x, y-wavevector components (see Eqs. (20) and (34) in reference [15]). However, the amplitude of both Φ_f^1 and Φ_f^2 are independent of the winding number α, and therefore, unlike the electrodynamic model, magnon excitation does not depend on vortex beam OAM. The discrepancy is likely caused by the atomistic vs. continuum nature of the two theories. A Heisenberg ferromagnet is modelled as a collection of discrete magnetic dipoles. Dipoles not at the centre of the vortex beam are subject to the mode broadening effect [21], where a range of OAM states are observed. On the other hand, in the continuum model the interaction is between the magnetic moment of the vortex beam and magnetisation of the sample [15]. It should also be noted that the Heisenberg description may not be valid for certain materials. For example, in metals the ferromagnetic state is due to the RKKY interaction between delocalised electrons [1], and in such cases it is not clear whether a discrete quantum model is entirely appropriate. Finally, the vortex results are only valid for thin crystals and kinematical scattering. For thicker crystals, the electron wavefunction within the specimen is altered by Bragg scattering [21], so that the winding number is no longer a good quantum number of the vortex beam.

The differential scattering cross-section $(d\sigma/d\Omega)$ for magnon excitation is given by [30]:

$$\frac{d\sigma}{d\Omega}=\left(\frac{k_f}{k_i}\right)|f_1(\theta,\phi)+f_2(\theta)|^2=\left(\frac{k_f}{k_i}\right)\left\{|f_1(\theta,\phi)|^2+|f_2(\theta)|^2+2\mathrm{Re}[f_1(\theta,\phi)f_2(\theta)]\right\} \tag{25}$$

The final term within the curly backets is due to interference of the

Φ_f^1 and Φ_f^2 scattered waves. For example, interference is zero for $k_{mx} = 0$, due to the phase shift between Φ_f^1 and Φ_f^2 being $\pi/2$ radians Eqs. (19) and (24). This highlights another important difference between the electrodynamic [15] and quantum mechanical models; the latter contains (partial) scattered waves which exhibit interference effects in the far-field. In the electrodynamic model however, the electron is treated as a particle, so that any wave-related phenomena, such as interference, is absent (see Eqs. (20) and (34) in [15] for electrodynamic cross-sections).

3. Magnetic diffuse scattering and delocalisation

In this section the magnon diffuse scattered intensity and interaction length scale with the incident electron beam is examined. For the former the simplest case of an electron plane wave incident along the optic axis is assumed, since the diffuse scattered intensity distribution in the diffraction plane is not complicated by any beam convergence, and interference effects are also absent. For a plane wave travelling along the optic z-axis, i.e. $\Phi_0(\mathbf{r}) = e^{2\pi i k_i z}$, only the $\partial/\partial z$ term in the magnetic transition potential is non-zero (Eq. (13)). From Eq. (15) the far-field scattering factor, $f_{\mathrm{pw}}(\theta,\phi)$, is:

$$f_{\mathrm{pw}}(\theta,\phi) = k_i k_{m\perp}\left(\frac{m\mu_0\mu_B^2}{\pi V_o \hbar^2 k_m^2}\right)\sqrt{\frac{2S(N_{km}+1)}{N_T}}e^{i\phi}\delta\left(\mathbf{k}_i - \mathbf{k}_f - \mathbf{k}_m\right) \tag{26}$$

The delta function and $e^{i\phi}$ terms signify linear and angular momentum conservation respectively. The differential cross-section is therefore [30]:

$$\frac{d\sigma_{\mathbf{k}m}}{d\Omega} = \left(\frac{k_f}{k_i}\right)\left|f_{\mathrm{pw}}(\theta,\phi)\right|^2 \approx \left(\frac{m\mu_0\mu_B^2}{\pi V_o\hbar^2}\right)^2\left(\frac{k_i k_{m\perp}}{k_m^2}\right)^2\left[\frac{2S(N_{km}+1)}{N_T}\right]\delta\left(\mathbf{k}_i - \mathbf{k}_f - \mathbf{k}_m\right) \tag{27}$$

where it is reasonably assumed that for small magnon energy losses $k_f \approx k_i$. The number of magnons N_{km} with wavevector $\mathbf{k}_m$ is given by the Bose-Einstein occupation factor. After integrating over the solid angle Ω, the scattering cross-section for the magnon is:

$$\sigma_{\mathbf{k}m} = \left(\frac{m\mu_0\mu_B^2}{\pi V_o\hbar^2}\right)^2\left(\frac{k_i k_{m\perp}}{k_m^2}\right)^2\left(\frac{2S}{N_T}\right)\left[\frac{1}{1-\exp\left(-\frac{\hbar\omega_m}{kT}\right)}\right] \tag{28}$$

where $\hbar\omega_m$ is the magnon energy. For a one-dimensional chain of atoms with periodic spacing 'a', $\hbar\omega_m = D_m[1-\cos(2\pi k_m a)]$, where D_m is a constant that depends on the exchange interaction [1]. To calculate the differential cross-section $d\sigma_{\mathrm{MDS}}/d\Omega$ due to all magnons, i.e. the magnon diffuse scattered intensity, the total scattering between polar angles θ to $(\theta + d\theta)$ must be incoherently summed. From the scattering geometry in Fig. 1b and conservation of energy, the following relationships must be simultaneously satisfied:

$$k_m^2 = k_i^2 + k_f^2 - 2k_i k_f \cos\theta \tag{29a}$$

$$\hbar\omega_m = \frac{h^2}{2m}\left(k_i^2 - k_f^2\right) \tag{29b}$$

For small energy losses, where $k_f \approx k_i$, Eq. (29a) reduces to a simple relationship between k_m and the scattering angle θ:

$$k_m = 2k_i\sin(\theta/2) \tag{30}$$

Consider Fig. 2a where circles of radii k_i and k_m are constructed around the start (O) and end (O') points of the incident wavevector $\mathbf{k}_i$. Since $k_f < k_i$, the scattering wavevector $-\mathbf{k}_m$ can, in principle, lie anywhere along the arc ABC. However, because of Eqs. (29a) and (29b), the scattering polar angle θ is fixed by the magnon wavenumber and energy, so that $-\mathbf{k}_m$ intersects the arc only at a fixed point B. Furthermore, for an isotropic solid the magnon energy depends only on the wavenumber k_m, and not the direction of the magnon wavevector. This means that the scattering vector can lie anywhere along the minor circle with radius $k_f\sin\theta$ passing through the points B and D (Fig. 2a). Now assume the polar angle is increased to $(\theta + d\theta)$. Using the trigonometric expansion of $\cos(\theta + d\theta)$ in Eq. (29a), and small angle approximation, it follows that the change dk_m in magnon wavenumber is $(k_i k_f/k_m)\sin\theta d\theta$. Multiplying by the circumference of the minor circle, the reciprocal space area due to scattering between angles θ and $(\theta + d\theta)$ is therefore $(k_i k_f^2/k_m)\sin\theta d\Omega$. From the Born-von Karman boundary conditions [31], a single magnon state in unit volume of solid will occupy a cube of dimension 2π in reciprocal space, so that there are approximately $[k_i k_f^2/(4\pi^2 k_m)]\sin\theta d\Omega$ number of magnon states that scatter within the desired range. This must be multiplied by the scattering cross-section for a single magnon (Eq. (28)) to obtain $d\sigma_{\mathrm{MDS}}/d\Omega$:

$$\frac{d\sigma_{\mathrm{MDS}}}{d\Omega} = \left(\frac{m\mu_0\mu_B^2 k_i}{2\pi^2 V_o\hbar^2}\right)^2\left(\frac{S}{2N}\right)\left[\frac{\cot^2(\theta/2)\cos(\theta/2)}{1-\exp\left(-\frac{\hbar\omega_m}{kT}\right)}\right] \tag{31}$$

where we have substituted $k_{m\perp} = k_f\sin\theta$ (Fig. 2a) and assumed small energy loss, i.e. $k_f \approx k_i$ and Eq. (30), to simplify the expression. Furthermore, since we are dealing with unit volume of solid, the total number of atoms N_T is replaced by the number density N. Eq. (31) assumes single magnon excitation and is therefore only valid for scattering angles within the first Brillouin zone. For small wavenumbers, $\hbar\omega_m \propto k_m^2 \propto \sin^2(\theta/2)$, so that the magnetic differential cross-section diverges at small scattering angles. In practice, the divergence at zero scattering angle is avoided, since the magnon wavevector must have a component normal to the z-axis in order to conserve angular momentum. Furthermore, at very small scattering angles the method used to count the number of magnon states is inaccurate, due to the reciprocal space area traced by the scattering vector being of a similar magnitude to the area occupied by a single magnon state (Born-von Karman boundary conditions).

The differential cross-section for single acoustic phonon thermal diffuse scattering for a crystal with monatomic basis can be derived using a similar procedure (see Supplementary Material):

$$\frac{d\sigma_{\mathrm{TDS}}}{d\Omega} = \left(\frac{m}{m_o}k_i^2 f_a(\theta)\right)^2\left(\frac{hN}{\pi M\omega_p}\right)\left[\frac{\sin^2(\theta/2)\cos(\theta/2)}{1-\exp\left(-\frac{\hbar\omega_p}{kT}\right)}\right] \tag{32}$$

where m_o, M are the electron rest mass and atomic mass respectively, ω_p is the phonon frequency and $f_a(\theta)$ is the atom scattering factor. For a one-dimensional chain of atoms with periodic spacing 'a', the acoustic phonon energy $\hbar\omega_p = D_p\sin(\pi k_p a)$, where k_p is the phonon wavenumber, and the constant D_p depends on the inter-atomic bond stiffness and atomic mass M [31]. For small wavenumbers, $\omega_p \propto k_p \propto \sin(\theta/2)$, and therefore the thermal differential cross-section approaches a non-zero value at small scattering angles. This is different to thermal diffuse scattering from a single atom [3], where the differential cross-section is zero at zero scattering angle. The discrepancy is likely due to inaccuracies in counting the number of phonon states at small scattering angles (recall previous discussion on magnons). To compare the relative magnitudes of magnetic and thermal diffuse scattering, Eqs. (31) and (32) are calculated for body centred cubic iron at room temperature for a 200 kV plane wave electron beam. Estimates for D_m and D_p were obtained from the small wavenumber region of magnon [14] and phonon [32] dispersion curves measured along the <100> crystallographic direction. A value of $S = 2.22$ was used based on the magnetic moment per ferromagnetic iron atom [1], while $f_a(\theta)$ was calculated from Kirkland's parameterisation [33].

Fig. 2b shows the magnetic and thermal differential scattering cross-sections plotted as a function of scattering angle. The former peaks at small scattering angles, while the latter increases monotonically for scattering angles within the first Brillouin zone. The two curves cross at ~0.5

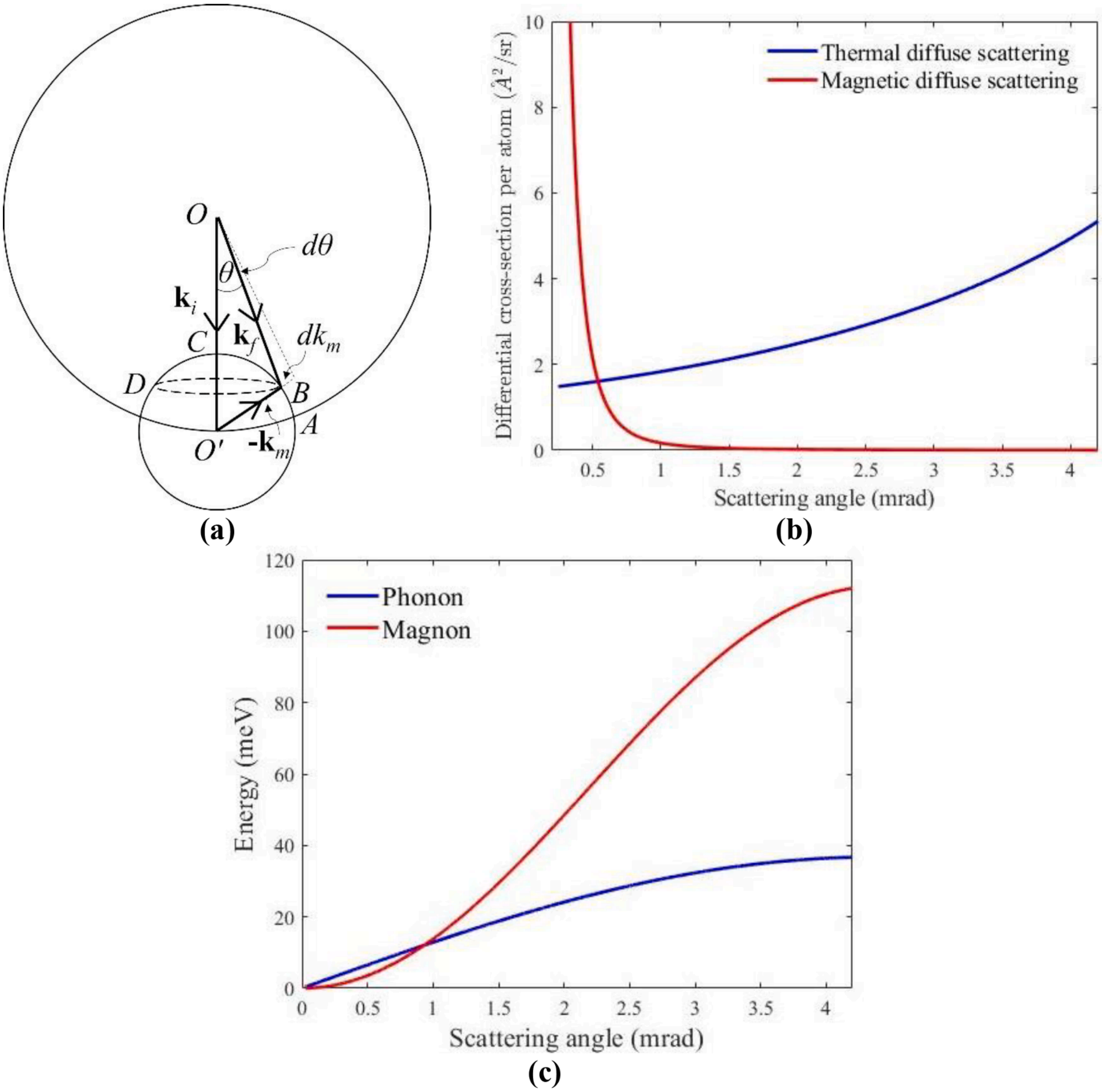

Fig. 2. (a) Schematic for calculating the number of magnon states scattering within the angular range θ to $(\theta + d\theta)$. $\mathbf{k}_i$ and $\mathbf{k}_f$ are the initial and final state wavevectors of the incident electron and $\mathbf{k}_m$ is the magnon wavevector. See text for further details. (b) Differential scattering cross-section for magnons and phonons in iron plotted as a function of scattering angle within the first Brillouin zone. The magnon and phonon differential cross-section per unit volume of solid Eqs. (31) and (32) is divided by the atom number density to give an average differential cross-section value per atom. (c) The magnon and phonon energies in iron plotted as a function of the scattering angle.

mrad scattering angle, where the magnon and phonon energies are 4.1 and 7.1 meV respectively, which is slightly below the energy resolution limit of current monochromated EELS [4]. Higher energy magnons are easier to resolve with EELS, but the lower scattered intensity places more stringent demands on the signal-to-noise ratio. For example, 30 meV magnons in iron have a differential scattering cross-section of 0.04 $\AA^2 sr^{-1}$ per atom, compared to 3.09 $\AA^2 sr^{-1}$ per atom for phonons of the same energy (see Fig. 2c for the magnon and phonon energies in iron corresponding to a given scattering angle). Fig. 2b also indicates that the reciprocal space region between the Bragg diffracted beams is largely due to thermal vibration of atoms, with the magnetic contribution being comparatively negligible.

The transition matrix element in Eq. (13) can be used to evaluate delocalisation between the electron beam and magnon during inelastic scattering. Representing the elastic and inelastic wavefunctions as $\Phi_0(\mathbf{r})\exp(2\pi i\mathbf{k}_i\cdot\mathbf{r})$ and $\Phi_f(\mathbf{r})\exp(2\pi i\mathbf{k}_f\cdot\mathbf{r})$ respectively, and after substituting in Eq. (6a), the inelastic amplitude due to magnon scattering within a slice of thickness Δz centred at depth z_o can be shown to be [34]:

$$\Phi_f(\mathbf{R}, z_o) = -i\sigma_f H^p_{f0}(\mathbf{R})\Phi_0(\mathbf{R}, z_o) \tag{33a}$$

$$H^p_{f0}(\mathbf{R}) = \int_{z_o-\frac{\Delta z}{2}}^{z_o+\frac{\Delta z}{2}} H_{f0}(\mathbf{r})e^{2\pi i(\mathbf{k}_i-\mathbf{k}_f)\cdot\mathbf{r}}dz \tag{33b}$$

where $\sigma_f = 2\pi me/(h^2 k_f)$ is the interaction constant for inelastic scattering, $\mathbf{R}$ is the two-dimensional position vector in the specimen *xy*-plane and $H^p_{f0}(\mathbf{R})$ is the transition matrix potential projected along the slice thickness. Eq. (33a) assumes small angle scattering, and that the wavevectors $\mathbf{k}_i$ and $\mathbf{k}_f$ are either parallel or nearly parallel to the optic *z*-axis. Furthermore, the Born approximation is assumed, i.e. the elastic wavefunction is the primary source of inelastic scattering. Substituting Eq. (13) in Eq. (33b) gives:

$$H^{p}_{f0}(\mathbf{R}) = \left(\frac{\mu_0\mu_B^2}{\pi e V_o k_m^2}\right)\sqrt{\frac{2S(N_{km}+1)}{N}}\int_{z_o-\frac{\Delta z}{2}}^{z_o+\frac{\Delta z}{2}} e^{2\pi i\left(\mathbf{k}_i-\mathbf{k}_f-\mathbf{k}_m\right)\cdot\mathbf{r}}\left[k_{mz}\left(\frac{\partial}{\partial y}-i\frac{\partial}{\partial x}\right)-\left(k_{my}-ik_{mx}\right)\frac{\partial}{\partial z}\right]dz \tag{34}$$

where N_T is replaced with the atomic number density N, since we are assuming unit volume of solid. Due to conservation of linear momentum the exponential term in Eq. (34) is equal to unity. Substituting in Eq. (33a) gives:

$$\Phi_f(\mathbf{R}, z_o) = -i\sigma_f\left(\frac{\mu_0\mu_B^2}{\pi e V_o k_m^2}\right)\sqrt{\frac{2S(N_{km}+1)}{N}}\left[k_{mz}\Delta z\left(\frac{\partial\Phi_0}{\partial y}-i\frac{\partial\Phi_0}{\partial x}\right)-\left(k_{my}-ik_{mx}\right)\int_{z_o-\frac{\Delta z}{2}}^{z_o+\frac{\Delta z}{2}}\left(\frac{\partial\Phi_0}{\partial z}\right)dz\right] \tag{35}$$

where it is assumed that $\Phi_0(\mathbf{r})$ is weakly dependent on z, so that $\partial\Phi_0/\partial x$ and $\partial\Phi_0/\partial y$ are both approximately independent of the depth over the infinitesimal slice thickness Δz. The integral in Eq. (35) can be evaluated by noting that in the Born approximation limit Φ_0 is largely governed by elastic scattering [33], i.e.:

$$\frac{\partial\Phi_0(\mathbf{R}, z_o)}{\partial z} = \left[\frac{i}{4\pi k_i}\nabla^2_{xy} + i\sigma_i V(\mathbf{r})\right]\Phi_0(\mathbf{R}, z_o) \tag{36}$$

where ∇^2_{xy} is the Laplacian in the xy-plane and $\sigma_i = 2\pi me/(h^2 k_i)$ is the interaction constant for elastic scattering. Substituting in Eq. (35) results in:

$$\Phi_f(\mathbf{R}, z_o) = [\theta_1(\mathbf{R}) + \theta_2(\mathbf{R})]\Phi_0(\mathbf{R}, z_o) \tag{37a}$$

$$\theta_1(\mathbf{R}) = -i\sigma_f\left(\frac{\mu_0\mu_B^2}{\pi e V_o k_m^2}\right)\sqrt{\frac{2S(N_{km}+1)}{N}}\Delta z\left[k_{mz}\left(\frac{\partial}{\partial y}-i\frac{\partial}{\partial x}\right)-\frac{i}{4\pi k_i}\left(k_{my}-ik_{mx}\right)\nabla^2_{xy}\right] \tag{37b}$$

$$\theta_2(\mathbf{R}) = -\sigma_f\sigma_i\left(\frac{\mu_0\mu_B^2}{\pi e V_o k_m^2}\right)\sqrt{\frac{2S(N_{km}+1)}{N}}\left(k_{my}-ik_{mx}\right)V_p(\mathbf{R}) \tag{37c}$$

where $V_p(\mathbf{R})$ is the crystal potential $V(\mathbf{r})$ within the slice at depth z_o projected along the z-axis direction. Following standard multislice procedure, $V_p(\mathbf{R})$ is approximated by linear superposition of the full projected potential of each atom within the slice [33]. Eq. (37a) indicates that there are two contributing factors to magnon excitation at a given specimen depth; a term $\theta_1(\mathbf{R})$ that depends on gradients in the xy-specimen plane of the elastic wavefunction $\Phi_0(\mathbf{R}, z_o)$, and a second term $\theta_2(\mathbf{R})$ that is proportional to the projected atomic potential of the crystal.

The magnon wavefunction (Eq. (37a)) generated within a 10 nm depth in [100]-oriented body centred cubic iron was calculated using multislice for both a plane wave incident along the optic z-axis and vortex beam [17,21] with 10 mrad semi-convergence angle and +1 winding number. The microscope accelerating voltage was 200 kV and all electron optic aberrations (i.e. defocus, spherical aberration etc) were set to zero. The multislice slice thickness was half the lattice parameter (i.e. 1.4 Å), and did not contain any phonon displacement of the atoms. Atom scattering factors were derived from Kirkland's parameterisation [33]. The magnon wavevector is parallel to [101] and has magnitude 8.7×10^8 Å^{-1}. This corresponds to a magnon energy of 56 meV, estimated using the magnon dispersion coefficient D_m for iron reported in [14].

Results for the electron plane wave are presented first. Fig. 3a shows the [100]-projected potential due to corner and body centred atoms, with a single unit cell of iron outlined for ease of visualisation. At the specimen entrance surface a plane wave propagating along the optic axis is uniform in the xy-specimen plane, so that $\theta_1(\mathbf{R})$ is zero and magnon excitation is due to $\theta_2(\mathbf{R})$ only. However, within a crystal the incident electron will undergo a series of channeling and scattering events, which result in a spatially non-uniform wavefunction. This is evident in Fig. 3b, which shows the modulus of the elastic scattered wavefunction at 10 nm specimen depth. $\theta_1(\mathbf{R})$ at this depth is therefore non-zero (Fig. 3c) and has intensity between the atom columns. $\theta_2(\mathbf{R})$ on the other hand, is localised to the atoms within the slice where magnon excitation takes place (Fig. 3d), which in this particular case happens to be the body centred atoms (cf. Fig. 3a). The maximum value for the $\theta_1(\mathbf{R})$ modulus is approximately seven times larger than that for $\theta_2(\mathbf{R})$. The magnon wavefunction $\Phi_f(\mathbf{R})$ is derived from both $\theta_1(\mathbf{R})$ and $\theta_2(\mathbf{R})$ (Eq. (37a)), and its modulus is shown in Fig. 3e. $\Phi_f(\mathbf{R})$ is seen to be similar to $\theta_1(\mathbf{R})$, with the comparatively weaker $\theta_2(\mathbf{R})$ term making only a small contribution. Magnon excitation is therefore delocalised away from the atom columns, even for a relatively thin (10 nm) sample. This is consistent with the recent magnon simulations of Lyon *et al.* [35].

Next consider the multislice results for a 10 mrad focussed vortex beam with +1 winding number. The vortex beam modulus at the specimen entrance surface is shown in Fig. 4a, and displays the characteristic singularity at the vortex centre as well as further zeros of the Bessel function. The spatial non-uniformity gives a non-zero $\theta_1(\mathbf{R})$, even at the specimen entrance surface. Electron channeling and scattering within a crystal gives rise to further inhomogeneities, which is evident from the modulus of the elastic wavefunction at 10 nm specimen depth (Fig. 4b).

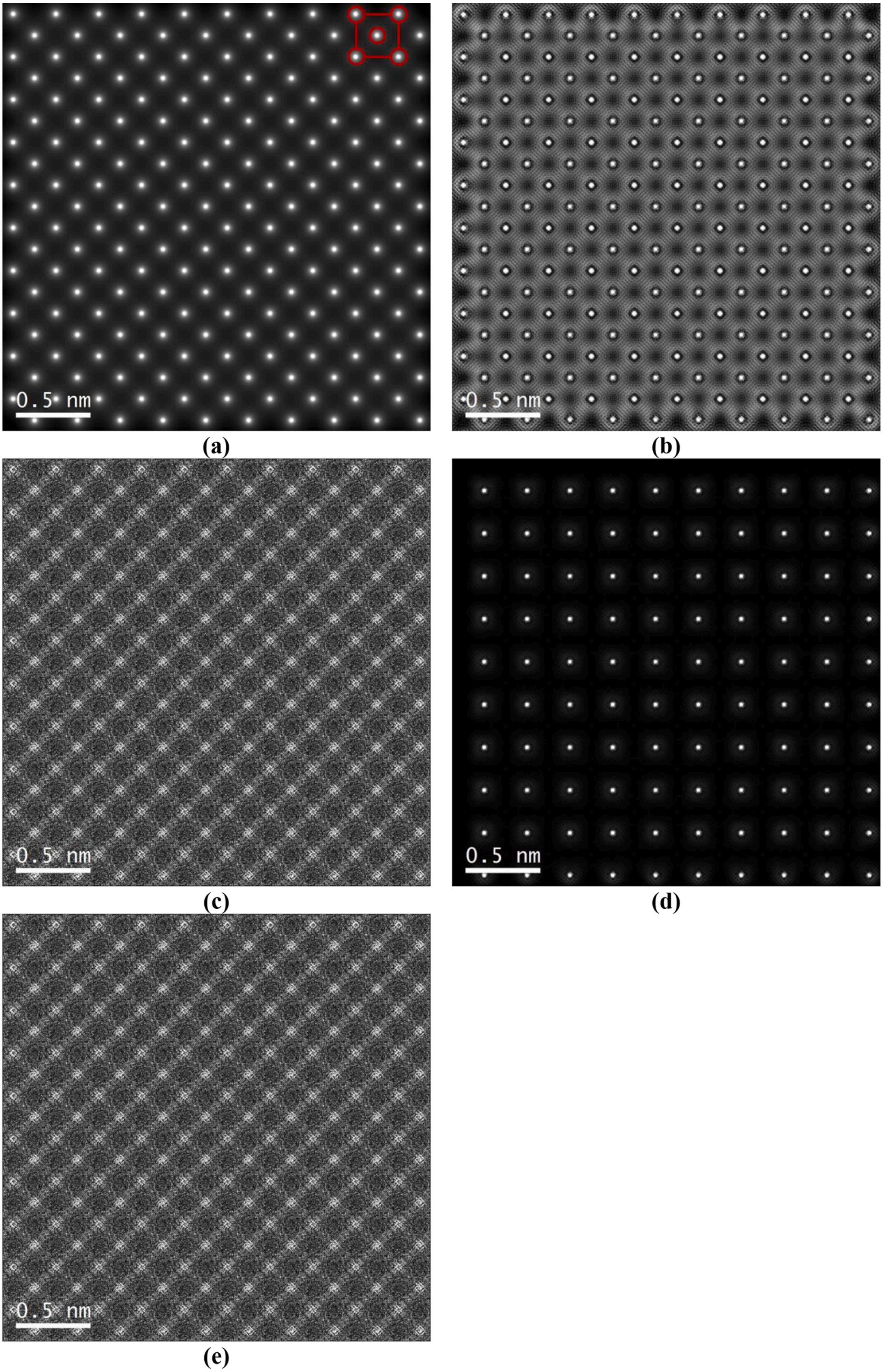

(a) (b) (c) (d) (e)

Fig. 3. (a) Projected potential of [100]-oriented body centred cubic iron. An outline of a single unit cell is superimposed in the top right-hand corner. (b) Modulus of the multislice simulated elastic wavefunction at 10 nm specimen depth for a 200 kV plane wave incident along the optic axis (electron optic aberrations, such as defocus and spherical aberration, are zero). The modulus of the $\theta_1(\mathbf{R})$ and $\theta_2(\mathbf{R})$ contributions to magnon excitation at this specimen depth are shown in (c) and (d) respectively, while (e) is the modulus of the magnon wavefunction.

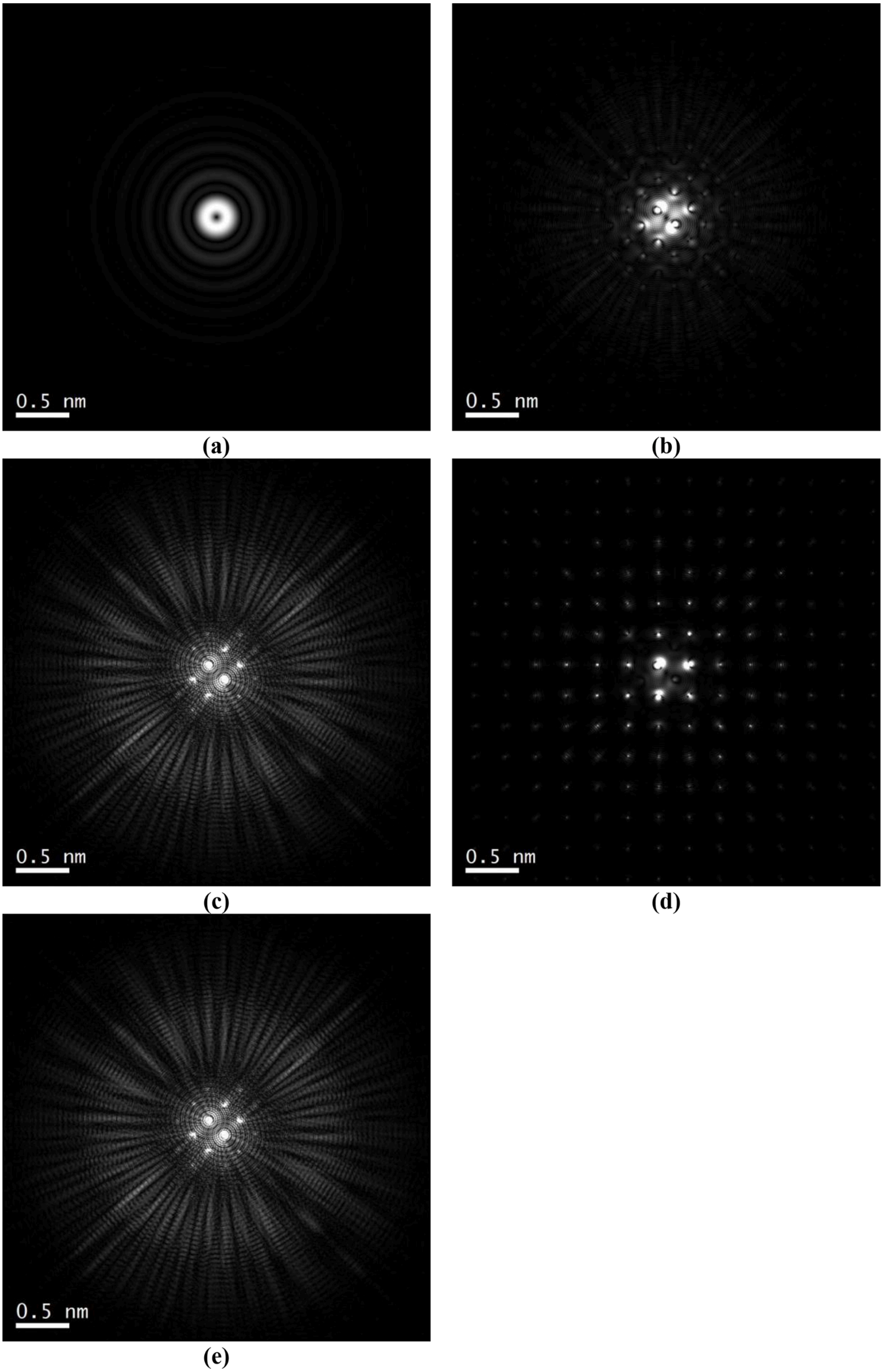

Fig. 4. (a) Modulus of a 200 kV, 10 mrad semi-convergence angle vortex electron beam with +1 winding number at the specimen entrance surface. Electron optic aberrations, such as defocus and spherical aberration, are zero. (b) Modulus of the multislice simulated elastic wavefunction for the vortex beam at 10 nm specimen depth in [100] body centred cubic iron. The modulus of the $\theta_1(\mathbf{R})$ and $\theta_2(\mathbf{R})$ contributions to magnon excitation at this specimen depth are shown in (c) and (d) respectively, while (e) is the modulus of the magnon wavefunction.

Because of dynamic scattering the vortex beam is no longer in a pure OAM state; the scattering mechanisms within a crystal and its effect on OAM mode broadening is described in detail in [21,36]. Moduli for $\theta_1(\mathbf{R})$ and $\theta_2(\mathbf{R})$ at 10 nm specimen depth are shown in Fig. 4c and d respectively, with the maximum value for $\theta_1(\mathbf{R})$ being approximately six times larger than that for $\theta_2(\mathbf{R})$. Consequently, the modulus of the magnon wavefunction (Fig. 4e) is similar to $\theta_1(\mathbf{R})$, indicating strong delocalisation for vortex beams as well.

These results can be compared with phonon excitation, where the interaction consists of delocalised 'dipole' and localised 'impact' scattering contributions [19]. The dipole contribution is dominant at small scattering angles, which is the experimental condition found in aloof beam scattering [19]. The multislice simulations presented here correspond to small angle scattering, where the $\theta_1(\mathbf{R})$ term is dominant, and, like dipole phonon scattering, is highly delocalised. This suggests that, similar to phonons, magnon excitations could be detected using focussed electron beams in an aloof EELS scattering geometry [37]. Long acquisition times are possible in aloof mode without inducing any specimen beam damage, an important pre-requisite for detecting potentially weak magnon signals. The aloof interaction is due to the long-range magnetic dipole field (Eq. (2)), which gives rise to a magnetic term in the Hamiltonian (Eq. (3)), or equivalently spatial gradients in $\theta_1(\mathbf{R})$. It is important however that the specimen is fully magnetised, i.e. single magnetic domain [1], so that the sample magnetic field penetrates into the surrounding vacuum region. The $\theta_2(\mathbf{R})$ term on the other hand is localised at the atom columns, and is therefore likely to be dominant at higher scattering angles. This suggests that, similar to phonons [6], atomic resolution magnon EELS spectroscopy should, in principle, be possible, although the weak intensity of magnetic diffuse scattering at higher angles (Fig. 2b) is an issue.

4. Conclusions

A Heisenberg ferromagnet consists of magnetic dipoles localised at individual atom sites. A high energy, spin unpolarised electron beam can interact with these dipoles through its orbital angular momentum. Vortex beams naturally have a net OAM, but even a plane wave can be decomposed into different OAM modes. For the former, atoms outside the vortex centre do not experience a pure OAM state, which should weaken the magnon interaction, since the magnon spin wave includes many such atoms. Despite this magnon inelastic scattering is still possible with vortex beams, although the cross-section is independent of vortex beam winding number. This is in stark contrast to EMCD, where the OAM mode broadening effect has been shown to suppress the magnetic signal for specimens larger than ~1 nm [22]. The result here is also different from a recently proposed electrodynamic model [15], where the magnon interaction increases with vortex beam OAM. The difference is likely due to the continuum nature of the electrodynamic calculation, where the vortex beam magnetic moment is assumed to interact with the sample magnetisation vector.

The magnon diffuse scattered intensity has also been quantitatively compared to phonon diffuse scattering for a 200 kV incident electron plane wave in iron. The magnetic diffuse intensity is dominant at small scattering angles (<0.5 mrad), but decays rapidly with scattering angle, such that the scattering cross-section for magnons that can be resolved by current state-of-the-art monochromated EELS is significantly smaller than phonons. This has two important implications. The first is that 'absorption' effects due to scattering between the Bragg beams is largely a thermal phenomenon, with any magnetic scattering playing only a minor role. The second is that the small cross-section makes magnon EELS spectroscopy extremely challenging. A potential solution might be to use focussed electron beams in aloof geometry, where the interaction is dominated by the long-range magnetic field of the atomic dipoles. Aloof incidence enables long counting times, while at the same time avoiding any beam induced specimen damage, an important criterion for detecting the weak magnon EELS signal.

Declaration of Competing Interest

The authors declare that they have no known competing financial interests or personal relationships that could have appeared to influence the work reported in this paper.

Supplementary materials

Supplementary material associated with this article can be found, in the online version, at doi:10.1016/j.ultramic.2022.113548.

References

[1] S. Blundell, Magnetism in Condensed Matter, Oxford University Press, Oxford, 2014.
[2] P.B. Hirsch, A. Howie, R.B. Nicholson, D.W. Pashley, M.J. Whelan, Electron Microscopy of Thin Crystals, Butterworths, Great Britain, 1965.
[3] S.J. Pennycook, D.E. Jesson, High-resolution Z-contrast imaging of crystals, Ultramicroscopy 37 (1991) 14.
[4] O.L. Krivanek, J.P. Ursin, N.J. Bacon, G.J. Corbin, N. Dellby, P. Hrncirik, M. F. Murfitt, C.S. Own, Z.S. Szilagyi, High energy resolution monochromator for aberration corrected scanning transmission electron microscopy/electron energy-loss spectroscopy, Phil. Trans. R. Soc. A 367 (2009) 3683.
[5] F.S. Hage, R.J. Nicholls, J.R. Yates, D.G. McCulloch, T.C. Lovejoy, N. Dellby, O. J. Krivanek, K. Refson, Q.M. Ramasse, Nanoscale momentum-resolved vibrational spectroscopy, Sci. Adv. 4 (2018) eaar7495.
[6] F.S. Hage, D.M. Kepaptsoglou, Q.M. Ramasse, L.J. Allen, Phonon spectroscopy at atomic resolution, Phys. Rev. Lett. 122 (2019), 016103.
[7] M.J. Lagos, A. Trügler, U. Hohenester, P.E. Batson, Mapping vibrational surface and bulk modes in a single nanocube, Nature 543 (2017) 529.
[8] M.J. Lagos, P.E. Batson, Thermometry with sub-nanometer resolution in the electron microscope using the principle of detailed balancing, Nano Lett 18 (2018) 4556.
[9] C. Dwyer, T. Aoki, P. Rez, S.L.Y. Chang, T.C. Lovejoy, O.L. Krivanek, Electron-beam mapping of vibrational modes with nanometer spatial resolution, Phys. Rev. Lett. 117 (2016), 256101.
[10] M.J. Whelan, Inelastic scattering of fast electrons by crystals II. Phonon scattering, J. Appl. Phys. 36 (1965) 2103.
[11] A.V. Martin, S.D. Findlay, L.J. Allen, Model of phonon excitation by fast electrons in a crystal with correlated atomic motion, Phys. Rev. B 80 (2009), 024308.
[12] B.D. Forbes, A.V. Martin, S.D. Findlay, A.J. D'Alfonso, L.J. Allen, Quantum mechanical model for phonon excitation in electron diffraction and imaging using a Born-Oppenheimer approximation, Phys. Rev. B 82 (2010), 104103.
[13] B.D. Forbes, L.J. Allen, Modelling energy-loss spectra due to phonon excitation, Phys. Rev. B 94 (2016), 014110.
[14] J.W. Lynn, Temperature dependence of the magnetic excitations in iron, Phys. Rev. B 11 (1975) 2624.
[15] B.G. Mendis, A semi-classical theory of magnetic inelastic scattering in transmission electron energy loss spectroscopy, Ultramicroscopy 230 (2021), 113390.
[16] J. Verbeeck, H. Tian, P. Schattschneider, Production and application of electron vortex beams, Nature 467 (2010) 301.
[17] P. Schattschneider, J. Verbeeck, Theory of free electron vortices, Ultramicroscopy 111 (2011) 14612.
[18] R.J. Elliot, R.D. Lowde, The inelastic scattering of neutrons by magnetic spin waves, Proc. Roy. Soc. A 230 (1955) 46.
[19] L.J. Allen, H.G. Brown, S.D. Findlay, B.D. Forbes, A quantum mechanical exploration of phonon energy-loss spectroscopy using electron beams in the aloof geometry, Microscopy 67 (2018) i24.
[20] J. Yuan, S.M. Lloyd, M. Babiker, Chiral specific electron vortex beam spectroscopy, Phys. Rev. A 88 (2013), 031801.
[21] B.G. Mendis, On the electron vortex beam wavefunction within a crystal, Ultramicroscopy 157 (2015) 1.
[22] P. Schattschneider, S. Löffler, M. Stöger-Pollach, J. Verbeeck, Is magnetic chiral dichroism feasible with electron vortices? Ultramicroscopy 136 (2014) 81.
[23] L.J. Allen, A.J. D'Alfonso, S.D. Findlay, Modelling the inelastic scattering of fast electrons, Ultramicroscopy 151 (2015) 11.
[24] B.G. Mendis, Theory underpinning multislice simulations with plasmon energy losses, Microscopy 69 (2020) 173.
[25] H. Yoshioka, Effect of inelastic waves on electron diffraction, J. Phys. Soc. Japan 12 (1957) 618.
[26] T. Holsten, H. Primakoff, Field dependence of the intrinsic domain magnetisation of a ferromagnet, Phys. Rev. 58 (1940) 1098.
[27] G.S. Adkins, Three-dimensional Fourier transforms, integrals of spherical Bessel functions, and novel delta function identities, 2022 arXiv:1302.1830v1 [math-ph].
[28] I.S. Gradshteyn, I.M. Ryzhik, Tables of Integrals, Series and Products, Academic Press, New York, 1980.
[29] P. Schattschneider, Exchange of angular momentum in EMCD experiments, Ultramicroscopy 109 (2008) 91.
[30] M. Inokuti, Inelastic collisions of fast charged particles with atoms and molecules-the Bethe theory revisited, Rev. Mod. Phys. 43 (1971) 297.
[31] N.W. Ashcroft, N.D. Mermin, *Solid State Physics*, Holt, Rinehart and Winston, 1976.

[32] V.J. Minkiewicz, G. Shirane, R. Nathans, Phonon dispersion relation for iron, Phys. Rev. 162 (1967) 528.

[33] E.J. Kirkland, Advanced Computing in Electron Microscopy, second ed., Springer, New York, 2010.

[34] W. Coene, D. Van Dyck, Inelastic scattering of high energy electrons in real space, Ultramicroscopy 33 (1990) 261.

[35] K. Lyon, A. Bergman, P. Zeiger, D. Kepaptsoglou, Q.M. Ramasse, J.C. Idrobo, J. Rusz, Theory of magnon diffuse scattering in scanning transmission electron microscopy, Phys. Rev. B 104 (2021), 214418.

[36] B.G. Mendis, Dynamic scattering of electron vortex beams - a Bloch wave analysis, Ultramicroscopy 149 (2015) 74.

[37] O.L. Krivanek, T.C. Lovejoy, N. Dellby, T. Aoki, R.W. Carpenter, P. Rez, E. Soignard, J. Zhu, P.E. Batson, M.J. Lagos, R.F. Egerton, P.A. Crozier, Vibrational spectroscopy in the electron microscope, Nature 514 (2014) 209.